A halo expansion technique for approximating simulated dark matter haloes

Ben Lowing,[★] Adrian Jenkins, Vincent Eke and Carlos Frenk

Department of Physics, Institute for Computational Cosmology, University of Durham, South Road, Durham DH1 3LE

ABSTRACT

We apply a basis function expansion method to create a time-evolving density/potential approximation of the late growth of simulated N-body dark matter haloes. We demonstrate how the potential of a halo from the Aquarius Project can be accurately represented by a small number of basis functions, and show that the halo expansion (HEX) method provides a way to replay simulations. We explore the level of accuracy of the technique as well as some of its limitations. We find that the number of terms included in the expansion must be large enough to resolve the large-scale distribution and shape of the halo but, beyond this, additional terms result in little further improvement. Particle and subhalo orbits can be integrated in this realistic, time-varying halo potential approximation, at much lower cost than the original simulation, with high fidelity for many individual orbits, and a good match to the distributions of orbital energy and angular momentum. Statistically, the evolution of structural subhalo properties, such as mass, half-mass radius and characteristic circular velocity, are very well reproduced in the HEX approximation over several Gyr. We demonstrate an application of the technique by following the evolution of an orbiting subhalo at much higher resolution than can be achieved in the original simulation. Our method represents a significant improvement over commonly used techniques based on static analytical descriptions of the halo potential.

Key words: methods: numerical – galaxies: haloes – dark matter.

1 INTRODUCTION

In the standard cosmological paradigm of structure formation (ΛCDM), dark matter haloes are built up through the repeated hierarchical merging of smaller haloes (White & Rees 1978; Frenk et al. 1985). These haloes provide the sites in which galaxies form. Any model of galaxy formation, be it an smoothed particle hydrodynamic simulation or a semi-analytical calculation, must include a description of the evolution of the halo in which the galaxy grows. These descriptions usually take the form of either N-body simulations, analytical potential profiles or statistical merger trees. In this paper, we present a new way of characterizing the evolution of dark matter haloes that can be employed in galaxy formation models or to explore their small-scale structure.

Nearly all representations of haloes are motivated by cosmological N-body simulations. These are a powerful tool and have allowed us to gain insight into the non-linear stages of halo growth. The initial power spectrum of density fluctuations in the CDM cosmogony has power on all scales and this affects the internal evolution of haloes on a wide range of scales. However, investigating the structure and substructure of haloes requires simulations

of ever-increasing resolution and ever-increasing computational expense. The state-of-the-art are the Aquarius simulations of galactic dark matter haloes, the largest of which achieved a resolution of $\sim 10^3\,M_\odot$ (Springel et al. 2008a). From these and other simulations (Stadel et al. 2009), we have learnt not only about the basic structure of haloes – that they have approximately universal density profiles well described by an NFW profile (Navarro, Frenk & White 1996, 1997) or that they are strongly triaxial in shape (Allgood et al. 2006; Bett et al. 2007; Hayashi, Navarro & Springel 2007) – but also about the properties of their small-scale structure (Diemand et al. 2008; Springel et al. 2008a; Vogelsberger & White 2011).

In spite of their impressive resolution, recent simulations have a number of limitations. First, only a few examples have been calculated so far. Secondly, their resolution is still below that required to follow the evolution of the smallest subhaloes, including those that host the ultrafaint dwarfs of the Milky Way. Finally, they neglect the effects of baryons in the evolution of the main halo and its subhaloes.

The high cost of full simulations can be avoided by introducing approximations. A commonly used one is to assume a static analytical potential to represent the halo and then perform a live simulation of just the small-scale component of interest. Computational resources can then be targeted at that component and large numbers of resimulations performed. This method has been applied

[★]E-mail: b.j.lowing@durham.ac.uk

to a wide range of problems, such as the orbits and evolution of sub-haloes (Taylor & Babul 2001; Zentner & Bullock 2003; Peñarrubia & Benson 2005), the build-up of galactic stellar haloes (Bullock & Johnston 2005), the formation of streams (Peñarrubia et al. 2006), or the disruption and heating of discs (Benson et al. 2004).

Using an analytical potential allows the parameters of the dark matter halo to be varied in a way that cannot be done in full *N*-body simulations. The major shortcoming of this approach is that representing the halo with a simple analytical potential is unrealistic. Although recent studies have assumed slightly more complicated forms for the potential, such as axisymmetric NFW profiles (Peñarrubia et al. 2006) or triaxial NFW profiles (Law, Majewski & Johnston 2009), they fail to include a realistic time-evolution, as haloes grow in stages through mergers, or to account for changes in triaxiality with radius (Hayashi et al. 2007) and time.

In this paper, we present a more advanced approach for representing the potential of a halo using a series expansion. Our approach is based on the formulation of the self-consistent field (SCF) method (Clutton-Brock 1973; Hernquist & Ostriker 1992, hereinafter HO). The SCF method involves describing a density field as a series expansion and then using this to self-consistently evolve the field. This is usually done by representing the density field as an *N*-body particle sampling and integrating the orbits of the particles in the series expansion potential. Previous work has used this method to perform *N*-body simulations (Weinberg 1996, 1999) and recently it has been applied by Choi, Weinberg & Katz (2009) to simulate the potential of subhaloes. SCF codes (also known as expansion codes) have the advantage of being efficient, of scaling linearly with the number of particles and of suppressing small-scale noise. It is desirable that the lowest order radial basis function resembles the system of interest so that a large number of terms are not required just to describe the basic density distribution. This can be avoided by tailoring the basis functions to the system by numerically solving the Strum–Liouville equation for the particular density distribution (Weinberg 1999). We have not done this in this paper; instead, for simplicity, we employ a radial basis function set based on the common simple analytical Hernquist halo profile (Hernquist 1990).

Rather than using the SCF method for the purpose of performing a complete simulation, we use just the series expansion part of the technique to approximate a pre-computed evolving density field, in this case a dark matter halo. This halo expansion (HEX) method offers us the means to create realistic approximations of an existing time-varying halo, which can then be employed for resimulations. Our approach has the distinct advantage of providing a much more realistic description of a halo potential than a simple static analytical form, while still being inexpensive. The starting point is a full *N*-body simulation. A set of coefficients are calculated that describe the halo with a chosen set of basis functions. Subsequently, an estimate of the halo density or potential at any point in space can be obtained by evaluating the appropriately weighted sum of the basis functions at that point. In addition, by calculating multiple independent sets of coefficients at various times in the halo's history and interpolating between the sets, we can describe the halo at any time during this period.

There is a wide range of possible applications of this method. It allows us to create approximations of very expensive halo simulations and then replay them at will. It can be used to study the evolving internal environment of the haloes or for the purpose of placing new objects into the simulations and observing their behaviour as if they had been present in the original simulation. Problems to which it is ideally suited include the orbits and stripping of subhaloes, the response of a light disc to the changing halo potential, the shape and precession of tidal streams, and the dynamics of satellites galaxies. In this paper, we focus on the first of these applications; we will explore the second in a later paper. Comparing orbits within a halo approximated by a series expansion to orbits calculated from the *N*-body halo serves as a demonstration of the method and provides a test of the accuracy of the approximation.

Limitations of our HEX technique include the lack of back reaction of the halo potential when new components are added. For example, if a model of a baryon disc is introduced, the associated reduction of triaxiality at the centre of the dark halo (Debattista et al. 2008; Abadi et al. 2010; Bett et al. 2010) cannot be included in the expansion approximation. At present, the method does not treat the effect of dynamical friction on objects orbiting within the halo. Although this can, in principle, be implemented in the method, Boylan-Kolchin, Ma & Quataert (2008) find that, for subhalo-to-halo mass ratios less than 0.1, the decay of the subhalo orbit due to dynamical friction over a few Gyr is small.

This paper is organized as follows. Section 2 describes the theory behind the HEX technique and how it has been applied to generate a representation of the density and potential of a simulated dark matter halo. Section 3 quantifies how well the approximation succeeds in recreating the orbits of both single particles and subhaloes. The latter part of the section carries out a comparison between the evolution of subhaloes in a full simulation and in the approximated potential. In Section 4, we use the expansion method for adding a new subhalo into the halo and finally, in Section 5, we summarize our conclusions.

2 METHODOLOGY

We start by presenting a brief overview of the theory behind our HEX method based on the SCF formulation and then describe the simulated haloes to which it has been applied and the considerations required in its application.

2.1 Basis function series expansions

The SCF method was originally devised by Ostriker & Mark (1968), where it was used to find the equilibrium structure of rapidly rotating stars. Clutton-Brock (1972, 1973) applied the SCF method to computational stellar dynamics to model the potential of simple galaxies. HO further developed the technique and it is upon their formulation we base this paper. The idea of the SCF technique is to expand the density and potential in a set of basis functions. The coefficients for the density can be found by summing over the particle distribution of a simulation. The corresponding coefficients for the potential are then obtained through solving Poisson's equation. Differentiation of the potential series gives the acceleration, which can then be used to self-consistently evolve the particles. We adopt the SCF method for creating a series expansion for an *N*-body distribution, but we do not use it to move the particles; instead, we are interested in the expansion itself.

We perform our expansion in spherical polar coordinates with r the radial distance, θ the polar angle and ϕ the azimuthal angle. We start by considering the potential and density written as the biorthogonal series

$$\rho(r, \theta, \phi) = \sum_{nlm} A_{nlm} \rho_{nlm}(r, \theta, \phi), \tag{1}$$

$$\Phi(r, \theta, \phi) = \sum_{nlm} A_{nlm} \Phi_{nlm}(r, \theta, \phi), \tag{2}$$

where $\rho_{nlm}(r, \theta, \phi)$ and $\Phi_{nlm}(r, \theta, \phi)$ are the basis functions labelled by n, l, m. A pair of biorthogonal series are defined by the property

$$\int \rho(\boldsymbol{r})_{nlm} \Phi(\boldsymbol{r})_{n'l'm'} \mathrm{d}\boldsymbol{r} = \delta_{nn'} \delta_{ll'} \delta_{mm'}. \tag{3}$$

If the individual basis function series are not orthogonal, then it is necessary to use a pair of biorthogonal series instead. When taking the overlap of the density with the potential basis functions, the biorthogonality property ensures that each coefficient only depends on a single potential basis function and that there is no contribution to it from any of the other basis functions. The basis functions are chosen so that each pair of terms are a solution to Poisson's equation

$$\nabla^2 \Phi_{nlm}(r, \theta, \phi) = 4\pi G \rho_{nlm}(r, \theta, \phi), \tag{4}$$

with G the universal gravitational constant.

While we have a free choice of basis functions, it is desirable that lowest order terms be a good approximation to the system being modelled. This reduces the need to expand to high order to obtain a good fit. We have adopted basis functions from HO, where radial basis functions are based on the Hernquist profile. A Hernquist profile is a reasonable fit to a dark matter halo, having an appropriate slope of r^{-1} at small radii but differing from the standard NFW form in its behaviour at large radii. For near-spherical distributions, it is natural to expand in spherical coordinates and use spherical harmonics. Equations (1) and (2) then become

$$\rho(r, \theta, \phi) = \sum_{nlm} A_{nlm} \rho_{nl}(r) Y_{lm}(\theta, \phi), \tag{5}$$

$$\Phi(r, \theta, \phi) = \sum_{nlm} A_{nlm} \Phi_{nl}(r) Y_{lm}(\theta, \phi), \tag{6}$$

where $Y_{lm}(\theta, \phi)$ are usual spherical harmonics. The zeroth-order radial basis function is just the Hernquist profile

$$\rho_{00} = \frac{1}{2\pi} \frac{1}{r} \frac{1}{(1+r)^3}, \tag{7}$$

with potential

$$\Phi_{00} = -\frac{1}{1+r}, \tag{8}$$

when written in dimensionless units where $G = 1$ and the scalelength in the Hernquist form $a = 1$. Higher order terms with $n = 0$ result from the assumption that they behave asymptotically as $r \to \infty$ as would a usual multipole expansion. To construct terms with $n \neq 0$, an additional radial function, $W_{nl}(\xi)$, is included, the form of which is found by inserting it into Poisson's equation. The transformation

$$\xi = \frac{r-1}{r+1} \tag{9}$$

maps r from the semi-infinite range to a finite interval and simplifies the following expressions. Following the derivation from HO, the final full set of potential and density basis functions are finally found to be

$$\rho_{nl}(r) = \frac{K_{nl}}{2\pi} \frac{r^l}{r(1+r)^{2l+3}} C_n^{(2l+3/2)}(\xi) \sqrt{4\pi} \tag{10}$$

and

$$\Phi_{nl}(r) = -\frac{r^l}{(1+r)^{2l+1}} C_n^{(2l+3/2)}(\xi) \sqrt{4\pi}, \tag{11}$$

where

$$K_{nl} = \frac{1}{2} n(n + 4l + 3) + (l+1)(2l+1) \tag{12}$$

and $C_n^{(2l+3/2)}(\xi)$ are the ultraspherical polynomials (Abramowitz & Stegun 1964). The expansions can then be rewritten in purely real quantities as

$$\rho(r, \theta, \phi) = \sum_{l=0}^{\infty} \sum_{m=0}^{l} \sum_{n=0}^{\infty} Y_{lm}(\theta) \rho_{nl}(r) (S_{nlm} \cos m\phi + T_{nlm} \sin m\phi), \tag{13}$$

$$\Phi(r, \theta, \phi) = \sum_{l=0}^{\infty} \sum_{m=0}^{l} \sum_{n=0}^{\infty} Y_{lm}(\theta) \Phi_{nl}(r) (S_{nlm} \cos m\phi + T_{nlm} \sin m\phi). \tag{14}$$

For a known density profile, the expansion coefficients S_{nlm} (or T_{nlm}) can easily be obtained by multiplying both sides of equation (13) by $[Y_{lm}(\theta) \Phi_{nl}(r) \cos \phi]$ (or $[Y_{lm}(\theta) \Phi_{nl}(r) \sin \phi]$) and integrating over all space. This needs to be modified for N-body simulations where the density field is represented by discrete particles. In this case, the integration over space becomes a sum over the particles, each weighted by its mass. Then, the expansion coefficients are

$$\begin{pmatrix} S_{nlm} \\ T_{nlm} \end{pmatrix} = (2 - \delta_{m0}) \tilde{A}_{nl} \sum_k m_k \Phi_{nl}(r_k) Y_{lm}(\theta_k) \begin{pmatrix} \cos m\phi_k \\ \sin m\phi_k \end{pmatrix}, \tag{15}$$

where

$$\tilde{A}_{nl} = -\frac{2^{8l+6}}{4\pi K_{nl}} \frac{n!(n + 2l + \frac{3}{2})[\Gamma(2l + \frac{3}{2})]^2}{\Gamma(n + 4l + 3)}, \tag{16}$$

r_k is the position of each particle and m_k its mass.

Once the coefficients are calculated, they can be used to evaluate equation (14) and find the potential at any location in space. Accelerations are obtained by differentiating the potential. By taking the gradient of equation (14), the accelerations can be written in spherical coordinates as

$$a_r(r, \theta, \phi) = -\sum_{l=0}^{\infty} \sum_{m=0}^{l} \sum_{n=0}^{\infty} Y_{lm}(\theta) \frac{\mathrm{d}}{\mathrm{d}r} \Phi_{nl}(r) \\ (S_{nlm} \cos m\phi + T_{nlm} \sin m\phi), \tag{17}$$

$$a_\theta(r, \theta, \phi) = -\frac{1}{r} \sum_{l=0}^{\infty} \sum_{m=0}^{l} \sum_{n=0}^{\infty} \frac{\mathrm{d}Y_{lm}(\theta)}{\mathrm{d}\theta} \Phi_{nl}(r) \\ (S_{nlm} \cos m\phi + T_{nlm} \sin m\phi), \tag{18}$$

$$a_\phi(r, \theta, \phi) = -\frac{1}{r} \sum_{l=0}^{\infty} \sum_{m=0}^{l} \sum_{n=0}^{\infty} \frac{m Y_{lm}(\theta)}{\sin \theta} \Phi_{nl}(r) \\ (T_{nlm} \cos m\phi - S_{nlm} \sin m\phi). \tag{19}$$

Both the radial and spherical harmonic basis sets are complete, so when summed from $n = 0 \to \infty$ and $l = 0 \to \infty$, the expansion converges to the exact distribution, although non-uniformly near discontinuities. However, in practice, the expansions are truncated at some high-order terms, $n_{\max}$ and $l_{\max}$. Truncated to a finite number of terms, equations (13) and (14) become

$$\rho(r, \theta, \phi) = \sum_{n=0}^{n_{\max}} \sum_{l=0}^{l_{\max}} \sum_{m=0}^{l} Y_{lm}(\theta) \rho_{nl}(r) (S_{nlm} \cos m\phi + T_{nlm} \sin m\phi), \tag{20}$$

$$\Phi(r, \theta, \phi) = \sum_{n=0}^{n_{max}} \sum_{l=0}^{l_{max}} \sum_{m=0}^{l} Y_{lm}(\theta) \Phi_{nl}(r) (S_{nlm} \cos m\phi$$
$$+ T_{nlm} \sin m\phi), \tag{21}$$

with the number of terms determining the accuracy to which the expansions reproduce the actual density distribution.

This algorithm is ideally suited to parallel computation. Each processor can independently calculate the coefficients for disjoint subsets of particles. A final summation collects together the contributions from each processor to generate the coefficients for the complete particle set. This ease of parallelism coupled with the algorithm being of $O(n)$ in the number of particles means it is ideally suited for use on huge data sets. However, the algorithm is to leading order $O(n_{max} l_{max}^2)$ for the number of basis terms included in the expansion and can quickly become computationally expensive if too many higher order terms are included.

2.2 Simulations

This work is based on a simulated Milky Way sized dark matter halo from the Aquarius Project (Springel et al. 2008a,b; Navarro et al. 2010). The Aquarius Project sample consists of six haloes of mass $\sim 10^{12}\,M_\odot$, which have each been resimulated at multiple resolutions. The simulations were performed using an improved version of GADGET (Springel, Yoshida & White 2001b; Springel 2005). The cosmological model used in the simulations assumes a ΛCDM cosmogony, with the parameters $\Omega_m = 0.25$, $\Omega_\Lambda = 0.75$, $\sigma_8 = 0.9$ and $n_s = 1$ and Hubble constant $H_0 = 73\,km\,s^{-1}\,Mpc^{-1}$. The six haloes were selected from the set of all isolated $\sim 10^{12}\,M_\odot$ haloes from a lower resolution 900^3-particle parent simulation of a $100\,h^{-1}$ Mpc box. Isolated means that a halo had no neighbours exceeding half its mass within $1\,h^{-1}$ Mpc; this ensured that the haloes were not members of any massive groups or clusters. Gravitationally bound substructures orbiting within the main larger Aquarius haloes are identified using the SUBFIND algorithm (Springel et al. 2001a).

The Aquarius Project haloes are ideally suited for this work as they are high-resolution simulations of single haloes, that have been carefully tested for convergence and have a large number of outputs saved at regular times. We have applied the HEX technique to two different resolution versions of the Aquarius A halo. The majority of this work is based on the higher resolution version known as Aq-A-2, while a lower resolution version, Aq-A-4, is used to check for convergence. Table 1 details the basic parameters of the simulations and haloes. There is a factor of 28 difference in the resolution of the two versions, with excellent convergence found between them. The Aq-A-2 simulation has a total of 1024 outputs, while the Aq-A-4 simulation has only 128. For this work, we have restricted

ourselves to the same 128 outputs from both versions, giving one approximately every 155 Myr at late times.

2.3 Application to simulated haloes

To apply the HEX technique to a dark matter halo from the Aquarius simulation, we expand about the potential minimum, as identified by SUBFIND by the most bound particle. A summation over all particles is performed, once for each halo, to yield a set of coefficients that describe the halo by the given basis functions. We limit the expansions to a small number of terms, resulting in a set of coefficients much smaller in comparison to the number of dark matter particles in the halo. This truncation of the series smoothes the density and removes small-scale detail.

Only particles within 1.3 virial radii of the halo centre are included in the coefficient summation. At greater distances, the distribution of material is more irregular and not well fitted by spherical basis functions. While the use of a hard cut-off at the boundary imposes a discontinuity in the density profile there, we find this not to be a problem. We have tested with larger as well as soft boundaries and find the exact choice makes little difference to our results. We choose to use a hard boundary for simplicity.

Fig. 1 shows the comparison of the density profile of the main halo from the Aq-A-2 simulation, obtained by binning the simulation
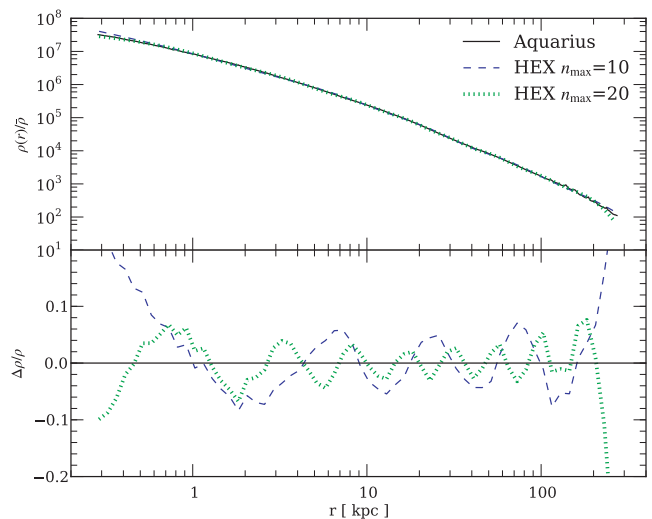

Figure 1. Upper panel: spherically averaged density profiles $\rho(r)$ of the main Aq-A-2 halo. The solid line is the profile of the actual halo from the simulation, while the dotted and dashed lines are the profiles from the expansion with $n_{max} = 10$ and 20, respectively. Bottom panel: residuals of the density profile fits, $\Delta\rho/\rho \equiv (\rho_{HEX} - \rho_{halo})/\rho_{halo}$, where ρ_{halo} is the true halo density and ρ_{HEX} denotes the HEX-approximated density.

Table 1. Basic parameters of the two Aquarius simulations of the A halo. m_p is the particle mass in the high-resolution region, ϵ_G is the Plummer-equivalent gravitational softening length, r_{200} is the virial radius, defined as the radius enclosing a mean overdensity 200 times the critical value, M_{200} is the mass within the virial radius and N_{200} is the total number of particles within r_{200}. Also listed is the position (r_{max}) of the peak (V_{max}) of the circular velocity profile.

Halo	m_p ($M_\odot$)	ϵ_G (pc)	r_{200} (kpc)	M_{200} ($M_\odot$)	N_{200} (10^6)	V_{max} (km s^{-1})	r_{max} (kpc)
Aq-A-2	1.370×10^4	66	244.84	1.842×10^{12}	134.47	208.49	28.14
Aq-A-4	3.929×10^5	342	245.70	1.838×10^{12}	4.68	209.24	28.19

particles into spherical shells, with its approximation by the HEX method. The lower panel shows the residuals between the model and the data. It can be seen that over the radial range 1–100 kpc, using just 11 radial basis functions, $n_{max} = 10$, the rms deviation of the residuals is 4.2 per cent, decreasing to 2.6 per cent when twice the number of radial terms, $n_{max} = 20$, are included. Even using just a few radial basis functions the expansion achieves a fit to within a few per cent to the spherically averaged density profile of the halo, over a range where the radial density varies by over six orders of magnitude.

2.3.1 Order of expansion

The accuracy of the approximation of the halo depends on the number of terms included in the expansion; the use of more terms allows smaller spatial features to be resolved. The spatial resolution approximately scales inversely proportional to n_{max} and l_{max}^2. The effect on the force of including more terms in the expansion can be seen in Fig. 2. Here, the radial component of the force for $n_{max} = l_{max} = 4, 9, 19$ and 39 is compared to the force as calculated directly from the original *N*-body simulation.

In the central region of the haloes, the radial force estimated from the expansion differs from that calculated in the simulations. The closer to the centre, the larger the disagreement. This divergence is due to the density of the simulated halo having a logarithmic slope shallower than -1, while the lowest order Hernquist basis function having a cusp at the centre with a slope of -1 and not being a good fit there. Excluding the centre from the comparison, so considering the region between 5 and 100 kpc, it is found that doubling both n_{max} and l_{max} from five to 10 terms results in a big improvement, with the fractional rms deviation falling from 4.8 to 1.3 per cent. Doubling the number of terms again gives further gains, with expansions using 20 and 40 terms resulting in the fractional rms deviations of 0.83 and 0.46 per cent, respectively.

As the expansion is taken to increasingly higher orders, the contribution of individual terms declines. Higher order terms resolve smaller scale structure, and eventually the very high order terms model only the shot noise from the discrete particle nature of the simulation. Following Weinberg (1996), we take the signal-to-noise ratio on a coefficient as $S/N \equiv [S_{nlm}^2/\mathrm{var}(S_{nlm})]^{1/2}$, where by consider-
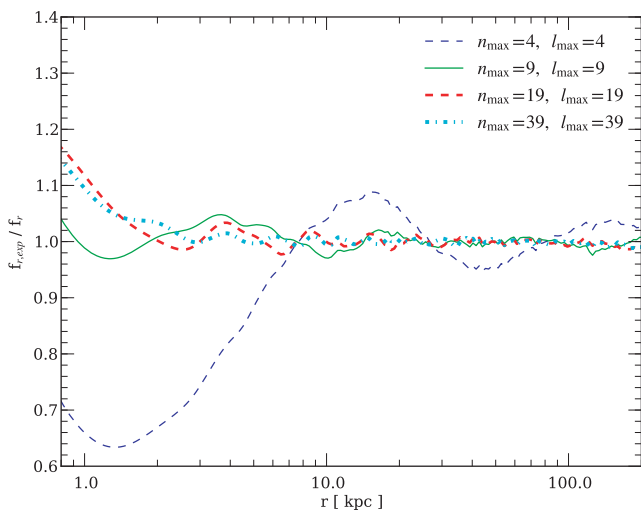

Figure 2. Radial component of the force calculated from the HEX approximation truncated at differing n_{max} divided by the actual force calculated directly from the Aq-A-4 simulation.

ing the computation of the coefficients as a Monte Carlo integration the variance can be estimated. *S/N* of less than 1 indicates that the particle distribution does not provide significant information on the value of that coefficient. We find that terms even of high order as $n_{max} = l_{max} = 20$ enjoy low levels of noise and contribute to resolving the halo structure. This is not surprising as the Aq-A-2 simulation has over 100 million particles within the virial radius, while an expansion with $n_{max} = l_{max} = 20$ contains only 8000 terms.

Gravity is a long-range force dominated by the large-scale distribution of material. The force on an object is therefore determined primarily by the overall distribution of mass, and resolving nearby small-scale fluctuations does not substantially improve the radial force estimate. Going to higher expansion orders is thus unnecessary, as long as we employ sufficient terms to resolve the large-scale structure. Additional terms do not provide much gain. A force accuracy of less than 1 per cent can be achieved using $n_{max} = l_{max} = 20$ and is sufficient for most purposes. We use expansions to this order in the rest of this paper.

2.3.2 Choosing the scalelength

The adopted set of basis functions contains a single free parameter corresponding to the scalelength, *a*, of their underlying Hernquist profile. This scalelength needs to be pre-determined and chosen so that the lowest order basis function is a good fit to the halo. We find that the accuracy of the expansion when approximating the force is fairly insensitive to the exact choice of scalelength. Examination of the rms deviation in the radial force as a function of scalelength shows that very small scalelengths give bad fits to the profile but any scalelength larger than 10 kpc is acceptable, with a minimum rms deviation at 33 kpc. As we have already seen, the lowest order basis function is not a good fit to the halo at the origin due to a mismatch in central slopes. Reducing the scalelength does not help this.

The basis functions are primarily constrained by the region where the number of particles per radial interval is a maximum. This occurs where the logarithmic slope of the density profile is -2, which is at the scalelength for an NFW profile and at half the scalelength for a Hernquist profile. It is in this region that we desire the lowest order basis functions to fit well in order to minimize the number of terms needed in the expansion. The Aquarius A halo is very well fitted at $z = 0$ by an NFW profile with a scalelength of 15.3 kpc. It is therefore unsurprising that the optimum scalelength for the best fit by the lowest order Hernquist basis function is found to be 33 kpc, approximately twice the the best-fitting NFW scalelength. Using this value obtains an average rms deviation in the radial force between 5 and 100 kpc of 0.53 per cent, with the force correct to within 3 per cent down to 2 kpc. In the rest of this paper, we use a scalelength of 33 kpc when modelling this halo.

2.3.3 Frame of reference

We perform the expansion in a frame moving with the halo. Haloes are accelerated by surrounding large-scale structure. In the simulation, this results in a halo having a peculiar velocity of several hundred km s^{-1}, a velocity comparable to the relative motion of the material within it. We wish to transform into a frame in which we can treat the halo as stationary. This will allow us to follow the relative motion of objects within a halo, such as the orbit of particles, and neglect the halo's movement through space in their equation of motion and not to take into account the position or the velocity of

the halo at intermediate times. Because of the halo's finite extent, this frame is not strictly an inertial frame, but is accelerating due to the gravitational effects of distant large-scale material. Since the material within the halo experiences the same acceleration, this is important only if there are significant differential tidal forces over the scale of the halo, but this is not the case; the long-range tidal force, calculated by direct summation, from distant material is less than 1 per cent the magnitude of the internal halo force within 100 kpc of the halo centre and can be safely ignored.

In order to transform into a stationary halo frame, we must define an origin that moves with the halo and remove the halo velocity. The origin of the halo frame is chosen as the halo potential minimum, x_{pm}. This is a well-defined point that follows a smooth path. The choice of the halo velocity to use for the transformation to a stationary frame is not obvious. We need to use the instantaneous halo velocity to make the correct transformation rather than the average velocity, which we could simply obtain from the motion of the potential minimum. A sensible choice is to look at the net motion of the material surrounding the potential minimum. We obtain a centre of mass velocity that corresponds to the potential minimum's velocity by selecting all particles within some bounding radius, R, of the halo centre. The velocity is then

$$v_c = \frac{\sum_i m_i v_i}{\sum_i m_i}, \qquad (22)$$

where i denotes all the particles that have $|x_i - x_{pm}| \leq R$. Restricting ourselves to the just inner region where the halo is almost static, we find that the exact choice of R makes little difference to the centre-of-mass velocity. Varying R between 1 and 20 kpc alters the velocity by less than a km s^{-1}. Including the entire halo gives a centre-of-mass velocity some 20 km s^{-1} different from that of the inner regions. We therefore choose to use the centre-of-mass velocity of the particles within 5 per cent of the virial radius, which for the Aq-A-2 simulation is $R = 12$ kpc at $z = 0$.

To show that this is a valid choice, we compare the orbits of particles integrated within the expansion with the orbits the same particles took within the original simulation. The next section describes this in detail. We find that for each subset of particles there is an optimal choice of velocity for the halo frame in which to integrate particle orbits in order to match their equivalent orbits from the Aquarius simulation. This velocity can be found through a minimization scheme, in which we attempt to minimize the difference in their final position compared with their position in the original simulation. While the optimum velocity depends on the set of particles considered, it only varies within a few km s^{-1} between cases, suggesting that the motion of the inner regions of the halo is almost uniform. A slight difference in motion throughout the halo is the cause of the small spread and allows us to define a window of several km s^{-1} in which we find that any choice of velocity for the halo frame works satisfactorily. Choosing a different velocity within this window changes the path of the orbital integration by only a per cent or two.

Not only does this show that an approximately stationary frame does exist, but we also find that the centre-of-mass velocity that we chose earlier lies within this window. This is true for the Aquarius A, B and C haloes and demonstrates itself to be a valid choice for the halo frame, especially as it can be easily determined in advance, whereas the optimum velocity for a particular case can only be located retrospectively. The resulting procedure for placing objects within the expansion approximation frame is to find their initial position relative to the halo potential minimum at the start time and their initial velocity with respect to the defined halo velocity, v_c.
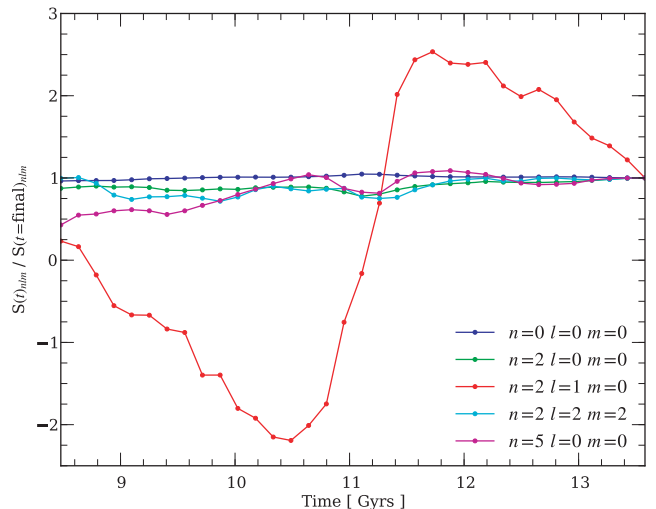

Figure 3. The variation of low-order coefficients as a function of time for the last 5 Gyr of the Aq-A-2 halo evolution.

The motion of the objects can then be followed totally within this frame and there is no need to further consider the overall motion of the halo.

2.3.4 Time-variation

Due to the fact that such a large amount of data is generated, the output of N-body simulations is usually recorded only at a few snapshots. Between these snapshots, information on the exact evolution of the halo is lost. However, it is usually sufficient to use simple interpolation to approximate it. The HEX technique is ideal for this because at each snapshot a new set of coefficients are calculated to describe the halo at that time. An approximation to the state of the halo at any intermediate time can be recovered by linearly interpolating the coefficient of each basis function between the directly preceding and following snapshots.

Fig. 3 illustrates the variation in a selection of low-order coefficients over the last 5 Gyr of the Aq-A-2 halo's growth, with a time-resolution set by the snapshot spacing of 155 Myr. The coefficient of the lowest order basis function varies very little, initially showing a slight increase until 11 Gyr, followed by a slight decline. The variation corresponds to the slight fluctuation in mass of the inner ∼100 kpc of the halo. The higher order coefficients have greater variation. The fluctuations on short time-scales, of the order of the time-spacing of the snapshots, are generally small, while the larger, more important, variations, such as the oscillation in the $n = 2$, $l = 1$, $m = 0$ coefficient, occur on longer time-scales. The time-spacing we use is sufficient to capture large-scale changes in halo structure. Smaller, quicker changes, such as those from substructure, may be missed but this does not matter as these are not spatially resolved by the expansion anyway.

3 RESIMULATING AQUARIUS

Once we have obtained a time-varying set of coefficients for a HEX approximation of an Aquarius halo potential and density, it is straightforward to use this to integrate orbits of test particles within the evolving halo potential. In order to test the accuracy of the HEX method, we examine how closely we can reproduce the properties of existing objects already present in the Aquarius simulations along their orbits. Based on the findings of the previous section, we use

a potential expansion including terms up to order $n_{max} = 20$ and $l_{max} = 20$, with a fixed scalelength of 33 kpc and summed over all particles within 340 kpc of the halo centre, to approximate the Aq-A-2 halo. A set of coefficients are generated for each snapshot, approximately every 155 Myr.

3.1 Integrating orbits

Ideally, if the potential is approximated accurately, test particles placed in the evolving halo potential will behave in the same manner as particles in the original simulation. This should be the case as long as the particles are not bound to any subhalo, since we are not attempting to resolve this level of detail. Therefore, by setting up a test particle with initial conditions matching the instantaneous state of a simulation particle and integrating the orbit within the HEX approximation, a comparison can be made between the path that the simulation particle actually followed and the one recreated using the HEX method. Differences in the orbital path or properties provide a guide to the accuracy of the HEX approximation.

Fig. 4 shows an example of an orbit that is particularly well reproduced. The orbit of the particle extracted from the Aq-A-4 simulation is compared with one integrated for 1 Gyr in the HEX potential. The recreated orbit closely matches the actual particle path, though it slightly diverges over time. By the end of the integration, there is some displacement between the final positions. While the orbit shape is well reproduced, the progress of the particles along their orbits is slightly out of phase. This discrepancy was introduced during the third apocentre passage, when the resimulated particle took a slightly wider orbit so that it subsequently lags behind the actual particle. An increasing divergence in paths is not unexpected as once a particle has even slightly different phase-space coordinates it will subsequently follow an increasingly different or-
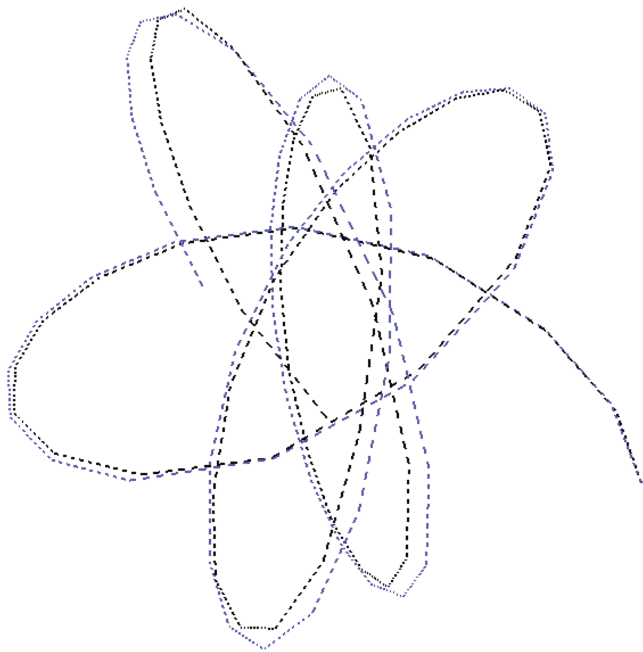

Figure 4. The orbit of a single particle in the Aq-A-4 simulation. The blue line shows the result of using the HEX approximation. The black line shows the actual path of the same particle followed through the Aquarius simulation. The particle positions were recorded only at limited points which have been joined by the straight lines. Both paths start from the same point on the right-hand side and are integrated for 1 Gyr.

bit. The energy of the two particles is matched to within 1.3 per cent throughout the entire orbit.

Once paths start to diverge, the particles will travel through different parts of the halo and it is therefore unsurprising that the properties of the original and recreated orbits become increasingly uncorrelated. It is more interesting to consider the properties of the particles over short time-periods, while the paths are still very similar. We do this for a set of 100 particles, randomly selected from the Aq-A-2 simulation from within 140 kpc of the halo centre at a redshift $z = 0.5$. We extract their orbits over 5 Gyr by finding their positions through 33 successive snapshots.

In order to compare the acceleration of these particles in the HEX approximation to the acceleration they experienced in the original GADGET simulation, we must remove the overall halo acceleration from the GADGET values. This is necessary as the integration in the HEX approximation is performed in a moving halo frame. The linear component of the overall halo acceleration is easy to remove and shows up as a systematic offset in the accelerations between the two cases. Calculating the mean acceleration difference in the final $z = 0$ snapshot finds a clear offset of 18.2 km s^{-1} Gyr^{-1}. Once this component is removed, we find a close match in the accelerations, with a median acceleration difference of 1.2 per cent for the 100 particles over 33 snapshots.

A comparison between the HEX approximation and a direct N-body force summation of the same material included in the HEX expansion gives a slightly better agreement for the median force differences of 0.9 per cent. The differences between this N-body summation and the GADGET force arise from a combination of the higher order acceleration components not being removed, possible errors in the force calculated by GADGET which come from a TreePM method, also an approximation, and the fact that the box containing the simulation is treated as periodic by GADGET. Regardless of these slight differences, both the comparison with the GADGET-calculated force and the direct summation demonstrate that there is in general an average force/acceleration error of approximately 1 per cent for the HEX approximation. In certain situations, there can be much larger errors; in one case, we find a difference of 90 per cent, when a particle comes within 500 pc of a large subhalo. Differences of this size are expected for the HEX potential near subhaloes, since such subhaloes are not well resolved in the approximation.

Integrating the orbits of the test particle set over the short time-period between snapshots allows us to measure the distance between the final positions and the actual particle positions in the Aquarius simulation. The integration is done by treating the particles as non-interacting and placing them at the same initial position with appropriate relative velocity, and using a simple drift-kick-drift leapfrog integrator with a fixed time-step of 1 Myr. By using the difference in forces at the snapshot times as an estimate for the average force error, we are able to calculate the expected divergence of orbits between snapshots and compare this with the divergence obtained from the HEX integration. Over the short time-scale between snapshots of ∼155 Myr, the displacements are small, usually a few hundred pc. We find that the error in the displacement of the integrated paths is consistent with the estimated error.

3.1.1 Energy changes

Examining how well the HEX approximation reproduces the integrals of the motion can be more indicative of differences in orbits than looking at the differences in the final position. Position is an instantaneous phase-space coordinate that rapidly varies along an orbit, and absolute differences in position are dependent on a
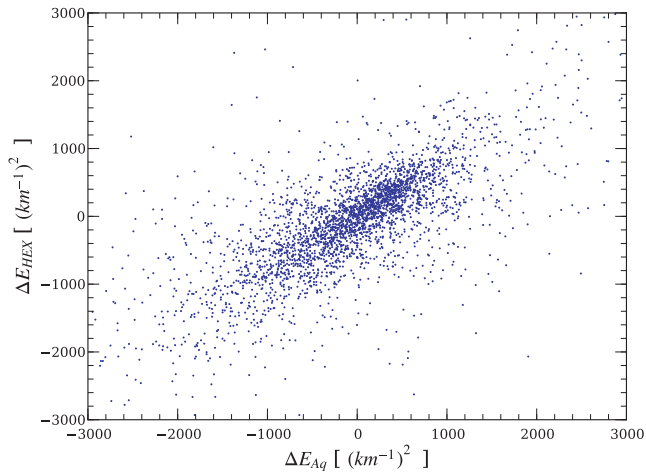
Figure 5. Energy change for selected particles between snapshots in the Aquarius simulation compared with the energy change for the same particles when their orbits are integrated over the same period in a HEX approximation of the Aq-A-2 halo.

particle's current radial distance from the halo centre. In contrast, energy, although not an integral of the motion since the potential is time-varying, changes slowly along the orbit. In a spherical potential, angular momentum would also be an integral of the motion. However, the Aquarius haloes are strongly triaxial, particularly in the centre, so contain a significant number of box-type orbits (Binney & Tremaine 1987). For these orbits, the angular momentum varies rapidly over very short time-scales, which makes a comparison between the Aquarius simulation and the orbits integrated in the HEX approximation less useful. In this section, we therefore only consider energy.

By again integrating the particle orbits between snapshot times in the HEX approximation, we can obtain a change in the orbital energy for each particle. We have checked that the change in energy is equal to the integral of the time-variation of the potential along the path to within 1 per cent. Using a smaller step size has a negligible effect on our results, confirming that the changes in energy are not due to the numerical integration. Fig. 5 shows the correlation between the changes in the particles' energy in the Aquarius simulation and their energy change in the integrated HEX potential. There is a clear correlation between the two cases, with a Pearson correlation coefficient of 0.75. The HEX approximation does well at reproducing energy changes even though the particles may not follow exactly the same paths. As well as path differences, the linear interpolation between coefficients will give a different variation in the potential at intermediate times; however, this does not seem to be important.

3.1.2 Encounters

Some of the test particles' orbits are significantly different from their Aquarius counterparts; they initially follow the Aquarius orbits but suddenly diverge and take very different paths. This occurs primarily for particles with low angular momentum on nearly-radial orbits. The pericentric passages of these orbits are very close to the centre of the halo. As the particles approach the centre, the separation distance between the reconstructed orbits and the Aquarius paths becomes of the same scale as the pericentric distance. The large relative path separation results in paths having substantially different approach angles and substantially different impact parameters, even in some

cases passing opposites sides of the centre. Since the centre is very strongly triaxial, the change in the angular momentum during the encounter with the non-spherical centre is sensitive to the direction of the incoming objects and will cause the pairs of particles to be diverted in radically different directions.

As well as the centre, which is responsible for the majority of these divergences, encounters with subhaloes can have a similar effect. Particles can either be deflected by subhaloes or become bound to them. To properly resolve a subhalo 1 kpc in size and 50 kpc from the centre would require at least an expansion with $n_{max} = 150$ and $l_{max} = 150$, over three million terms.

3.1.3 Population distribution

Even though individual orbits integrated in the HEX approximation may not always match their counterparts, the overall distributions of the energy and the magnitude of the angular momentum are well reproduced. This can be seen in Fig. 6, the distribution of total energies of 10 000 randomly selected test particles, and in Fig. 7, the distribution of the magnitude of the orbital angular moment. Both figures include the initial distributions and the final distributions from both the original Aquarius simulation and HEX resimulation over 5 Gyr.

The final energy distributions are very similar. A Kolmogorov–Smirnov (K–S) test gives a probability of 0.24 that the energy distributions are drawn from the same parent distribution. Therefore, the null hypothesis that the energy distributions of the orbits from the Aquarius simulation and HEX resimulation are the same is not rejected at a statistically significant level. There is equally good agreement for the angular momentum, with a 0.42 K–S test probability. The very similar distributions suggest that while individual orbits may not be exactly reproduced, there is no systematic difference in orbits integrated in the HEX approximation and those found in the Aquarius simulation. There is, however, a significant difference between the final and initial distributions, with a K–S test probability of less than 1.3×10^{-12} that the samples of orbital energies are drawn from the same distribution. The halo is accreting new material and evolving over the period of consideration, changing the overall distribution of energy. The fact that we match
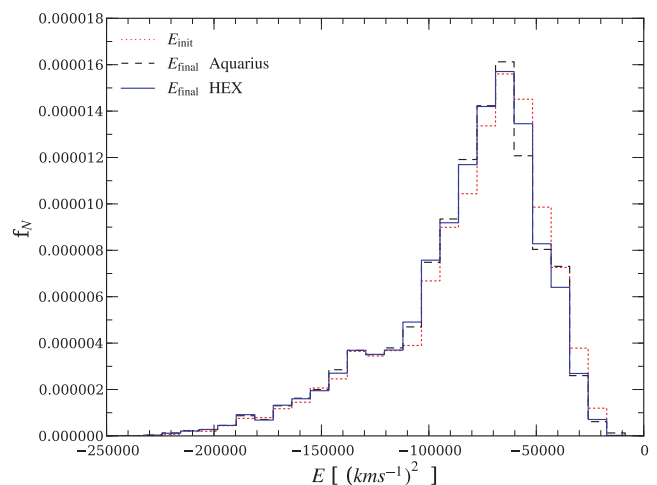

Figure 6. The distribution of the total energies of the 10 000 test particles. The dotted line shows the initial energy distribution, while the dashed line is the distribution of their energies in the simulations after 5 Gyr. The solid line is the energy distribution in the HEX resimulation.
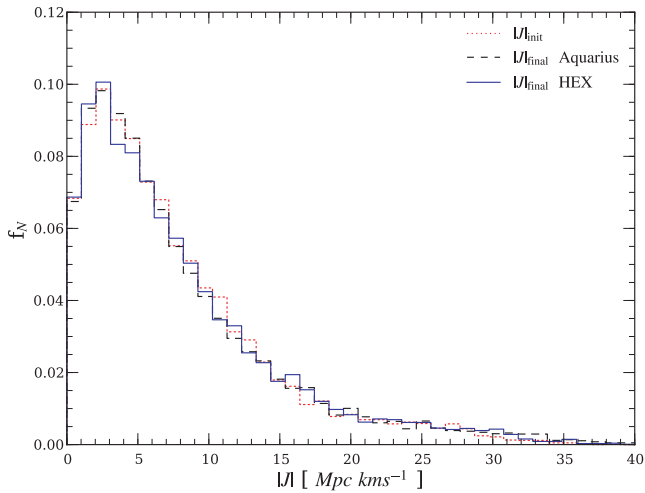
Figure 7. The distribution of the magnitude of the angular momentum of the 10 000 test particles. The dotted line shows the initial distribution, while the dashed line is the distribution in the Aquarius simulations after 5 Gyr. The solid line is the distribution in the HEX resimulation.

the final simulation distribution using the HEX approximation clearly demonstrates that the method correctly reproduces this evolution.

Focusing on orbits confined near to the centre of the parent halo, we find an even better match than ones with larger apocentric distances. This is a consequence of both the fact that the basis functions used in the HEX approximation have lower spatial resolution at larger radii and thus structure is not resolved as clearly in the outer regions, and the fact that the halo is dynamically older and more stable towards the centre. Restricting our attention to particles confined to a region near the centre of 3–20 kpc, where the HEX expansion is very successful, selects particles on near-circular orbits. When we consider the energy and angular momentum distributions for these orbits, we find that there is little evolution in the distributions, with significant K–S probability of 0.14 for energy and 0.76 for angular momentum that the population properties of the initial and final simulations have not changed. There is also very good agreement between the HEX and the simulation distributions, 0.97 for energy and 0.37 for angular momentum. Orbits in this region are of particular interest when considering galactic discs.

3.2 Subhaloes

Having studied the orbits of individual particles, we now turn our attention to the dynamics and evolution of subhaloes. These are large, gravitationally bound, extended bodies undergoing tidal evolution as they orbit within the parent halo. We compare the orbits of subhaloes resimulated within different HEX potentials, treating the subhaloes as extended objects, with the orbits of subhaloes from the Aquarius simulation. To model a subhalo as an extended body, we select the subhalo from the Aquarius simulation and identify all the particles that SUBFIND assigns to it. The same particles are extracted from subsequent snapshots and SUBFIND is run on just this particle set to calculate those that are still gravitationally bound. This results in a complete orbital path and record of the subhalo's evolutionary history. The resimulation of the subhaloes is done using a version of GADGET modified to allow additional HEX external potentials. The subhaloes are composed of multiple particles allowed to interact gravitationally. From the Aq-A-2

simulation, we selected all 1507 subhaloes with 100 or more particles that are within 90 kpc of the centre of the parent halo at $z = 0.5$. Their orbits and evolution are then integrated for 5 Gyr in the HEX potential.

The contribution to the potential from a subhalo needs to be removed from the halo expansion that is used to resimulate its orbit. Not excluding the self-contribution would lead to a double counting of the subhalo, because the gravitational effects of the subhalo are already included in the potential expansion. The double counting would generate an unrealistic self-attraction to the resimulated counterpart. Since the coefficients are just linear sums, it is easy to remove the contribution from the subhalo by separately calculating the coefficients of just the subhalo particles from the original simulation and subtracting them from the total coefficients. This does not remove the entire presence of the subhalo from the HEX approximation, as the halo response (i.e the dynamical friction wake) is still part of the expansion. While a resimulated subhalo closely follows the same orbit as in the original simulation, the wake can be an additional source of drag. However, an estimate of the dynamical friction on a subhalo based on the Chandrasekhar model (Chandrasekhar 1943) shows that it is negligible for the majority of subhaloes and only really important for the most massive ones.

In contrast, there can be no new halo response to the subhaloes in the resimulation, due to the fixed nature of the expansion; therefore, there is no direct dynamical friction on the subhaloes. This is a potential limitation of the HEX technique, but if necessary dynamical friction could be added to the equation of motion. To do so would require an estimate of a subhalo's size and mass, which information is not easily available until the simulation is post-processed by SUBFIND or unless some subhalo evolutionary model is assumed. Since the majority of our samples are small subhaloes of mass $\sim 10^6 \, M_\odot$, the dynamical friction from both effects can therefore be discounted as a significant source of error in reproducing subhalo orbits.

The success of recreating orbits of subhaloes resimulated within a full HEX approximation is similar to that of single particles; most orbits are very well matched while others are not. We find that there is minimal difference between the orbits of subhaloes when treated as point masses and when treated as extended bodies. Over 99 per cent of subhaloes have a difference of less than 10 per cent (82 per cent less than 1 per cent) in their final energy when treated as a point mass rather than as an extended object, and over 90 per cent have a difference of less than 10 per cent (43 per cent less than 1 per cent) in their final radial distance from the centre. This suggests that the extended nature of the subhalo has a minor effect on its motion, even though mass is being continuously stripped from the subhalo, forming leading and trailing streams.

The cases where the Aquarius subhalo orbits and the resimulated orbits dramatically differ are again the result of encounter events. Subhaloes encounter the centre of the parent halo in the same way as particles, and any slight differences in the orbits are greatly amplified during the pericentric passage. However, as well as the passages near the centre, subhalo encounters are found to be more frequent than for single particles. When two subhaloes strongly interact, the orbit of at least one of the pair can be completely changed. In particular, a large subhalo merging into the parent halo will scatter any small subhaloes it passes as it falls in. These subhalo–subhalo interactions are not well reproduced in the subhalo simulations using the HEX approximation, since, while contributions to the potential from subhaloes are included, these are not well enough resolved with the number of basis functions we use to model them. Instead, the potential from subhaloes is blurred out.

3.2.1 Evolution

As subhaloes orbit within their parent halo, they are tidally stripped and shocked, losing mass and decreasing in size. Exactly how subhaloes evolve and their final fate is a problem that has been extensively studied (Peñarrubia & Benson 2005; Angulo et al. 2009). We resimulate subhaloes in three different potential expansions corresponding to differing levels of sophistication. The simplest is a fixed, spherically symmetric Hernquist potential, an example of an analytical potential that is commonly used to represent dark matter haloes in simulations (Adams & Bloch 2005; Bullock & Johnston 2005). The second is a HEX potential that includes only radial basis functions to obtain the correct radial mass distribution, but with no information about the shape of the halo. The final potential is a full HEX potential including both radial and angular terms. We use the three different potentials in order to assess the difference between the evolution of subhaloes using the commonly employed method with a static simple potential and the effect of using a full time-varying triaxial approximation.

The parameters for the Hernquist potential are chosen so that it matches the lowest order basis function from the expansion of the halo at $z = 0$. It has a scalelength of 33 kpc and a total mass of $2 \times 10^{12} \, \mathrm{M_\odot}$. This is a good fit to the halo at the final time but overestimates the mass at earlier times. The second potential (HEX$_R$), using only radial terms, has $n_{max} = 20$ and $l_{max} = 0$, with a scalelength of 33 kpc and has time-varying coefficients. The full potential (HEX$_{20}$) uses the default parameters, so it has $n_{max} = 20$ and $l_{max} = 20$, is also time-varying and has a scalelength of 33 kpc. Again, we exclude the contribution to the HEX potential from the resimulated subhaloes.

We start by focusing on a single subhalo to illustrate the technique in more detail. This subhalo has been selected from the Aq-A-2 simulation and contains 13 120 particles, with a total mass of $1.8 \times 10^8 \, \mathrm{M_\odot}$. The subhalo was selected at redshift $z = 0.5$ and resimulated for 5 Gyr, with output snapshots every 155 Myr. It is compared to the same subhalo extracted at the same times from the Aq-A-2 simulation.

Fig. 8 shows the radial distance of the subhalo from the centre of the potential and three main structural properties that describe the state of a subhalo: the mass, the maximum circular velocity and the half-mass radius. The properties of the subhaloes in the two simplest methods, the Hernquist potential and HEX$_R$, immediately diverge from that of the Aquarius simulation, as a consequence of the fact that they follow different orbits, as may be seen in the top panel. These different orbits cause the subhalo to experience different tidal stripping and, at pericentre, different amounts of tidal shocking, resulting in incorrect estimates of the structural properties. In the HEX$_{20}$ resimulation, the subhalo follows an orbit very closely matching the actual subhalo's orbit for the first 2.5 Gyr, until, following the first pericentric passage, the orbits begin to diverge. Subsequently, the Aquarius subhalo reaches a greater apocentric distance and falls back in slightly later. Following this, near the halo centre, the small differences in the paths are sufficiently large that during the second passage the HEX$_{20}$ resimulated subhalo and the original Aquarius subhalo pass the centre on opposite sides and depart in different radial directions.

During the initial period while the orbit of the subhalo in the HEX$_{20}$ resimulation closely follows the fiducial Aquarius orbit, the subhalo properties, the mass, half-mass radius and maximum circular velocity, are reproduced extremely well. The subhalo is stripped and distorted in the same manner as in the Aquarius simulation. The subhalo continuously loses mass as it orbits within the parent
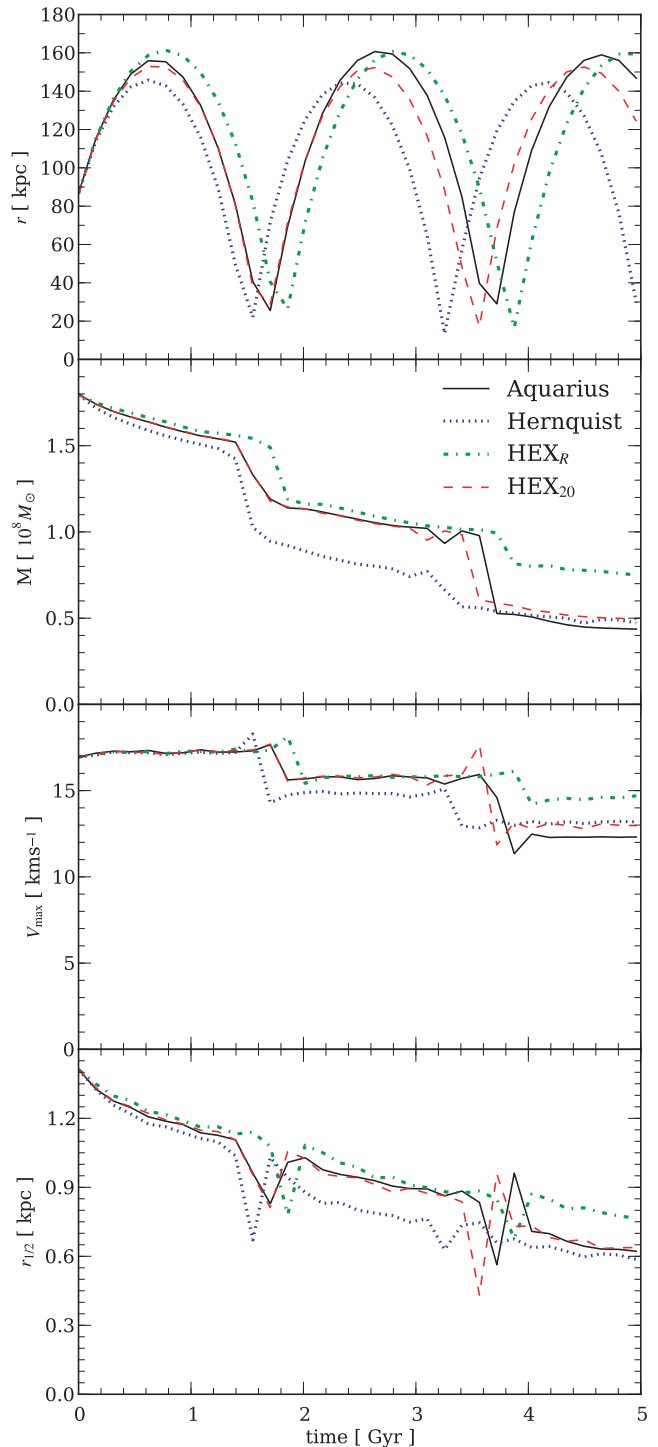

Figure 8. Comparison between the properties of different versions of the same subhalo. The full Aquarius Aq-A-2 simulation is represented by the black line. The other lines show resimulations of the subhalo in three differing potentials. Upper panel: the distance of the subhalo from the centre of the parent halo. Upper middle panel: the mass of the subhalo. Lower middle panel: the maximum circular velocity. Bottom panel: the half-mass radius.

halo, with sudden and large decreases during pericentric passages. Similarly, the maximum circular velocity, which is determined by the mass in the inner regions of the subhalo, is unaffected as mass is stripped from the outer edge. It is only when the subhalo makes
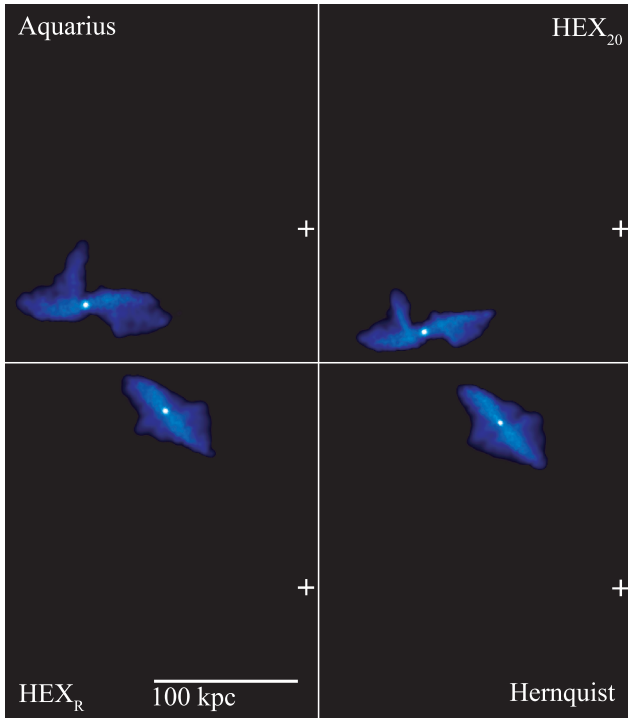
Figure 9. A projection of the smoothed density of a single subhalo resimulated in different potential approximations at the subhalo's second apocentre. The subhalo reaches the second apocentre at different times in the resimulations. The cross marks the centre of the parent halo in each case. Upper left-hand panel: the subhalo at 2.6 Gyr in the original Aquarius simulation. Upper right-hand panel: the subhalo at 2.6 Gyr in the full HEX_{20} potential. Lower left-hand panel: the subhalo at 2.8 Gyr in the HEX_R potential. Lower right-hand panel: at 2.3 Gyr in a static Hernquist potential.

a close approach to the parent halo centre and is tidally shocked and subject to maximum tidal stripping that the internal structure of the subhalo is notably changed. This behaviour is seen both in the Aquarius simulation and the HEX_{20} resimulation and indicates that the important gravitational mechanisms – tidal stripping and shocking, responsible for the evolution of a subhalo – are equivalently modelled by the full HEX potential as they are in the full simulation.

An instantaneous picture of the subhalo during its second apocentre can be seen in Fig. 9. Rather than comparing the subhalo at the same time, it is fairer to compare it at the same position along the orbit as this removes any difference in orbital phase. The resimulated subhalo in the HEX_{20} potential is strikingly similar to the original Aquraius subhalo. It is close to the correct position at the correct time and has very similar tidal tails. This similarity includes the small perpendicular protrusion to the left-hand side of the subhalo, which is a result of the end of the trailing tidal tail being broken off during the apocentric turnaround. In contrast, there is little resemblance between subhaloes in either the Hernquist or the HEX_R resimulation and in the Aquarius original, though there is strong resemblance between the two simulations. Both potentials are spherical, confining the subhalo to orbit in a plane, and thus the two potentials generate similarly shaped orbits. However, there is a large phase difference between the two. The Hernquist subhalo reaches the second apocentre 290 Myr before the Aquarius subhalo, while the HEX_R subhalo reaches the second apocentre 140 Myr after the Aquarius subhalo.

The final values of the mass, maximum circular velocity and half-mass radius are similar in the Hernquist and HEX_{20} resimulations, but this is more a coincidence than the result of the subhalo having the correct evolution in the Hernquist potential. While not completely correct, the evolution of the subhalo is much closer to the real case when the full HEX potential is used than when the simplified potentials are used. This suggests that both the radial mass distribution and the angular shape of the halo are important for reproducing correct orbits, which is a prerequisite to achieve similar evolution.

3.2.2 Population evolution

To assess whether the evolutionary mechanisms on subhaloes are the same even though the orbits may not exactly match, we now consider a population of subhaloes and look at the statistical match between a set of Aquarius reference subhaloes and resimulations of them in the three potentials. From the Aq-A-2 simulation, we again use the set of selected subhaloes with 100 or more particles that are within 90 kpc from the centre of the parent halo at $z = 0.5$. The particles belonging to these subhaloes are then tracked forward in time to follow the subhaloes' evolution in the full simulation.

Fig. 10 shows the population distribution of the three main structural properties of subhaloes: the mass, the half-mass radius and the maximum circular velocity. The distribution of the ratios of the final to the initial property has been used to remove the influence of the property distribution and allow an easier comparison of the actual evolution that the subhaloes undergo during 5 Gyr. The distribution of mass ratios shows how much stripping the subhaloes experience. Nearly all subhaloes in the Aquarius simulation lose mass over the 5 Gyr but a small fraction gain mass. The gain in mass can be explained by intersubhalo mergers, where two or more subhaloes join to form a larger subhalo. The HEX resimulations and the Aquarius simulation have the same small fraction of suhaloes undergoing this mass increase; they have similar distributions of mass ratios, with the same wide spread and a peak that occurs at 0.65. Only the Hernquist potential shows significant difference.

Similarly, the half-mass radius distribution is well matched by the resimulations, except again by the Hernquist potential which is slightly shifted to smaller sizes. Even though subhaloes generally lose mass, a small proportion grow in size. This can occur when a subhalo passes the pericentre and is tidally shocked by the rapidly changing potential field, thus increasing its internal energy and resulting in an increase in size. This occurs in both the Aquarius simulations and HEX resimulations. The maximum circular velocity distribution is slightly smaller in all the resimulations, with the largest discrepancy again for the Hernquist population. The primary reasons why the results from the Hernquist resimulation are so different from the other two are the assumption of a static potential of fixed mass throughout the whole simulation, which overestimates the actual mass of the Aquarius halo at early times, and the fact that a Hernquist potential gives the incorrect tidal radius for subhaloes. The tidal radius is the distance from the centre of a subhalo at which the gravitational tidal pull from the parent halo is equal to the pull from the subhalo itself. The material outside this radius is stripped from the subhalo and becomes part of the parent halo. We find that the Hernquist potential leads to underestimates of the tidal radius for subhaloes that are between 30 and 200 kpc from the centre of the parent halo and to overestimates outside this range. The subhaloes therefore experience a different rate of stripping over the course of
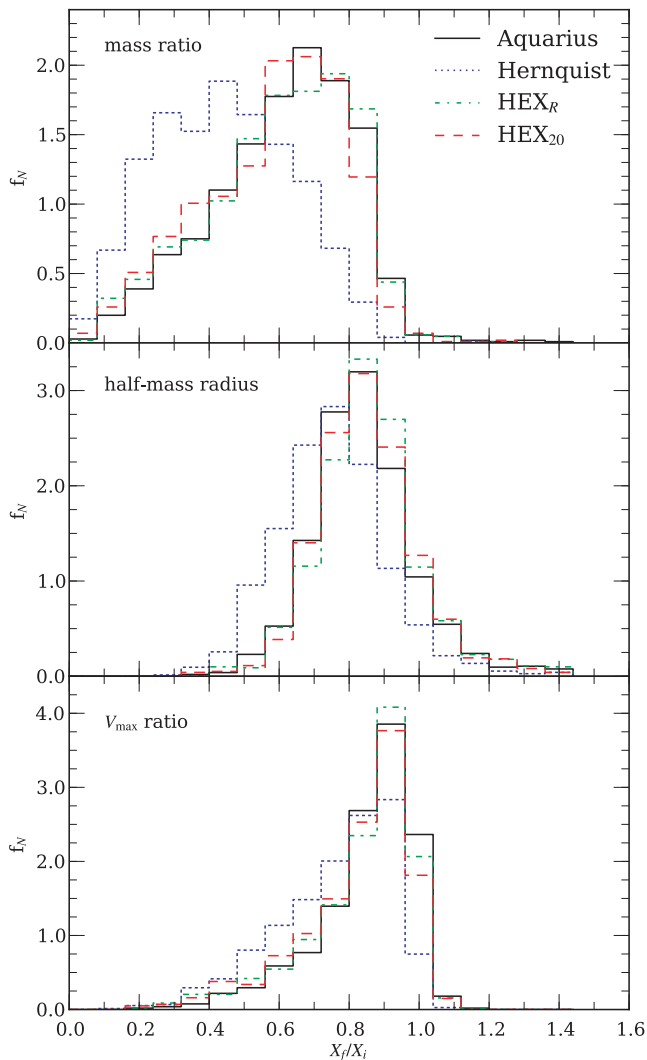
Figure 10. The distribution of X final over X initial for a selected Aquarius subhalo population for three different physical properties. The black line shows the actual distribution that occurred in the original Aquarius simulation, while the other colours correspond to the different resimulations. For each subhalo, the ratio is the given property at $z = 0$ compared to its initial value at $z = 0.5$. Upper panel: the distribution of final-to-initial mass ratios. Middle panel: the distribution of the final and initial half-mass radii. Bottom panel: the distribution of the final and initial maximum circular velocities.

their orbits than they do in the original simulation and the other cases.

Since the HEX$_R$ potential achieves an equally good match to the Aquarius simulation as the full HEX potential that also includes the angular terms, we conclude that the shape of the potential is unimportant for reproducing the structural evolution of the subhalo population in a statistical sense; only the radial mass distribution needs to be correctly reproduced. The stripping of mass from a subhalo is controlled by the tidal radius of the subhalo; thus, reproducing this property correctly ensures correct overall evolution. This can be done by matching the radial mass distribution, which is easily achieved with a small number of basis functions. In order to obtain similar evolution on an individual subhalo basis, the orbits need to be well matched, which does require the angular distribution and the full HEX approximation.

4 APPLICATION

Having shown that the orbits, as well as the subhalo evolution, are similar in a HEX approximation and in the original simulation, we now demonstrate how the HEX technique can be used to go beyond the original simulation. The introduction of new objects into the halo that were not present in the original simulation allows us to investigate the reaction of these objects as if they had evolved in a cosmologically realistic potential. They are unable to induce a back reaction on the halo, but the method is appropriate for studying light objects that would have had little effect on the halo. This can be achieved at a much lower cost than re-running a complete simulation and is more realistic than assuming a fixed analytical profile, such as a Hernquist profile.

4.1 Increasing subhalo resolution

We now illustrate the technique of placing new, additional subhaloes into the potential and simulating them at much higher resolution. As a test, a subhalo is constructed to be similar to the subhaloes found in the simulations, with an NFW density profile

$$\rho(r) = \frac{\rho_0}{\left(\frac{r}{r_s}\right)\left(1 + \frac{r}{r_s}\right)^2}, \tag{23}$$

with $\rho_0 = 8 \times 10^7 \, \mathrm{M_\odot \, kpc^{-3}}$ and $r_s = 0.27 \, \mathrm{kpc}$, and an isotropic velocity distribution. The subhalo is injected into the HEX potential approximation of the Aq-A-2 halo. To create equilibrium N-body halo realizations, we have used the algorithm described in Kazantzidis, Magorrian & Moore (2004) based on sampling the phase-space distribution function to generate the subhalo. Since the mass of an object with an NFW profile does not converge with radius, we truncate the subhalo at the virial radius using an exponential cut-off with a decay length set to 10 times the virial radius. This ensures the subhalo has a finite mass.

We generate the initial subhalo at two resolutions. The first, lower resolution version consists of 6000 particles with masses of $1.4 \times 10^4 \, \mathrm{M_\odot}$, the same particle mass as the Aq-A-2 simulation. The second version contains 10^6 particles with individual particle masses of just $82 \, \mathrm{M_\odot}$ and a resolution 170 times higher. Since the subhalo is small, with the SUBFIND mass of $5 \times 10^7 \, \mathrm{M_\odot}$, the absence of dynamical friction should not be significant. The subhalo is placed 190 kpc from the halo centre, approximately at the virial radius of the parent halo, where it will be just entering into the main halo and would not yet have been significantly stripped. The subhalo is simulated from $z = 0.5$ for 5 Gyr.

The orbits of the two different resolution versions of the subhalo are virtually identical. This is not unexpected, as we have already found that subhaloes orbit as point masses regardless of their extended nature. The changes in the properties of the subhalo over the 5-Gyr simulation are shown in Fig. 11. Here we compare the evolution of the mass, maximum circular velocity and half-mass radius between the low- and high-resolution simulations. While both realizations of the subhalo are sampled from identical NFW profiles, the initial SUBFIND mass is slightly higher for the low-resolution version. Later mass estimates agree, suggesting that in both cases the subhalo was stripped to the same tidal radius and the same material was lost regardless of whether SUBFIND had initially associated it with the subhalo or not.

The maximum circular velocities again are very slightly different, but the higher resolution version has a smoother evolution since it is less affected by the noise from the discrete particle nature of the subhalo. The half-mass radius has the same initial discrepancy
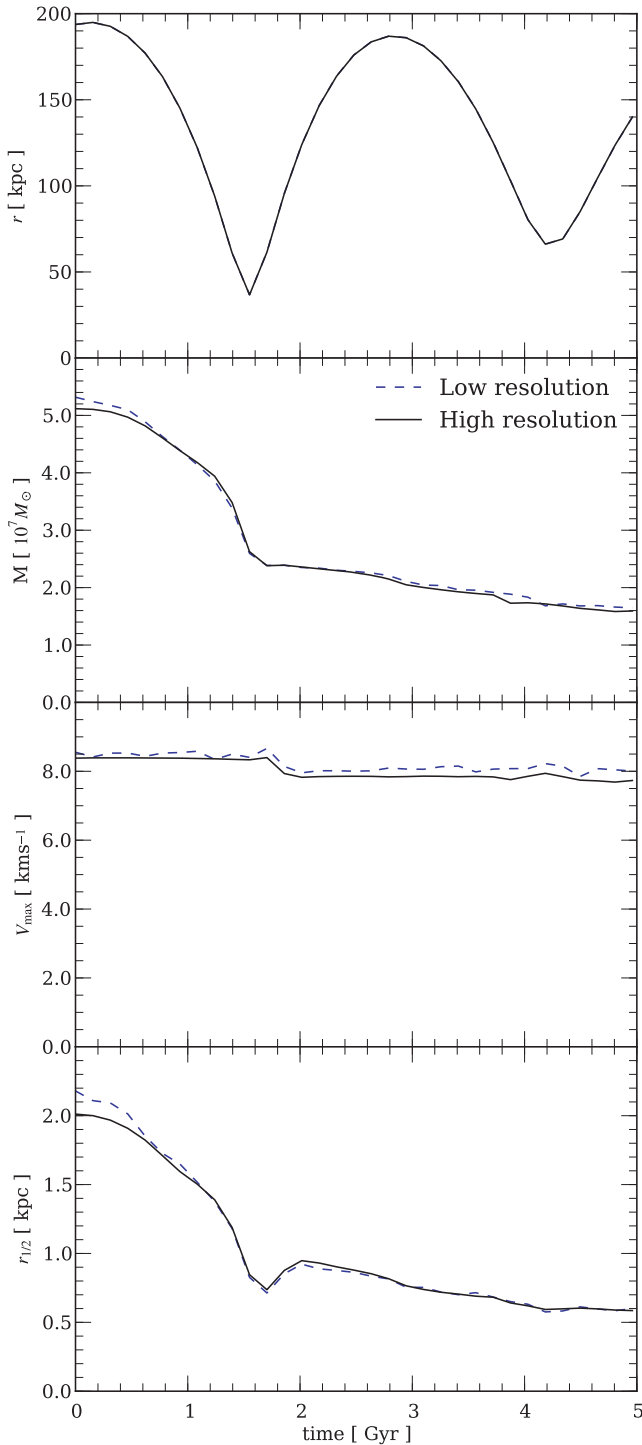
Figure 12. The smoothed density of the resimulated subhalo after 5 Gyr at $z = 0$ using the HEX potential. Upper picture: the low-resolution realization subhalo containing 6000 particles. Lower picture: the high-resolution realization subhalo containing 10^6 particles.

Apart from studying the subhalo, we can compare the fate of the material that is stripped from it and forms streams. There is both a leading stream and a trailing stream, containing material that is no longer bound to the subhalo but continues to follow similar orbits. These streams match in the high- and low-resolution simulations but are much clearer and can be traced much further in the high-resolution version. Sections of the streams containing a few tens of particles in the low-resolution version are now populated with thousands of particles in the high-resolution simulation. Features that had been only hinted at are clearly defined in the high-resolution simulation. Especially clear are the caustics of the streams which can be seen in Fig. 12. Another feature that is not resolved in the low-resolution simulation but is clearly visible in the high-resolution version is the bifurcation into two separate arms of the leading tidal tail, the one above the subhalo in Fig. 12.

The HEX method allows us to simulate a subhalo at different resolutions, with clear convergence between the two cases we have examined. By focusing computing resources on just the subhalo and using an approximation to the potential of the larger parent halo, we have been able to reach an unprecedentedly high resolution, using a particle mass of a few tens of solar masses and resolving tidal streams much farther and in a much sharper way than has been previously achieved. The low-resolution simulation required only 15 CPU hours[1] and the high-resolution subhalo only 2700 CPU hours. This is small compared to the Aquarius A level 2 simulation, which has a resolution equivalent to the low-resolution subhalo and

[1] On a 2.2-GHz AMD Opteron (AMD Opteron 175).

Figure 11. Comparison between the properties given by SUBFIND for a subhalo simulated for 5 Gyr at two resolutions in the HEX potential. Upper panel: the distance of the subhalo from the centre of the parent halo. Upper middle panel: the mass of the subhalo. Lower middle panel: the maximum circular velocity. Bottom panel: the half-mass radius.

as the mass, but again agrees at later times, with both versions undergoing the same compression of the subhalo during the first pericentric passage. Overall there is excellent convergence between the two resolutions and it is clearly demonstrated that the structural evolution is independent of the resolution of the subhalo as expected.
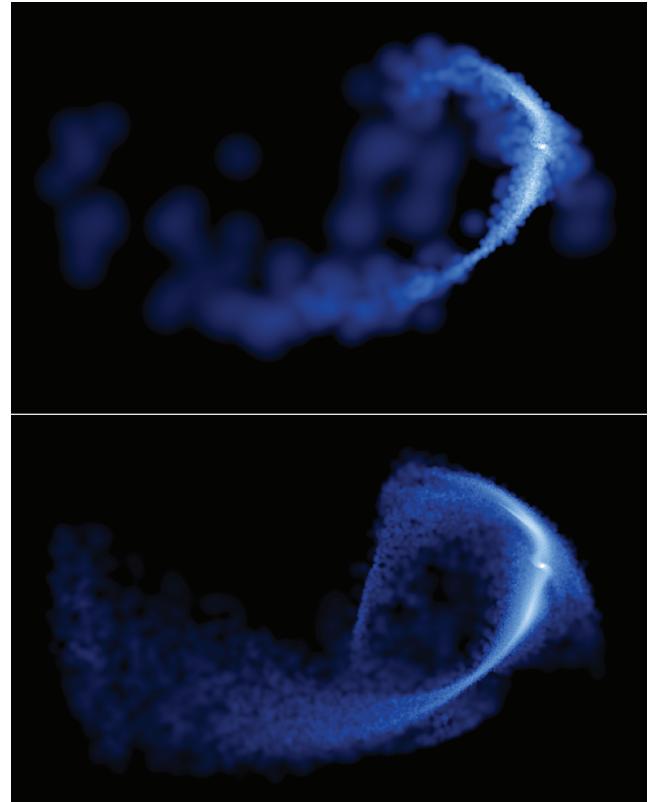
which took of the order of ~150 000 CPU hours over the same time-interval. While a full simulation may include thousands of subhaloes, we have demonstrated that is is possible to vary the parameters and re-run multiple versions of a single subhalo in a small fraction of time.

5 CONCLUSIONS

We have demonstrated the power of using the HEX method to approximate a dark matter halo. While much work has previously been carried out using expansion methods as part of the SCF technique to calculate the force in an *N*-body simulation, this is the first time that an expansion technique, such as the HEX technique, has been applied to describe an already simulated dark matter halo. Using a small number of basis functions, the HEX technique offers a way to approximate the time-evolving potential. A set of coefficients can be calculated once from the simulation and then serve as a realistic approximation of a halo. It is simple to integrate orbits within the HEX potential approximation and, as a first test, we focused on particle and subhalo orbits.

Using the HEX method to represent a dark matter halo, however, has some limitations. The potential is fixed and unable to react to objects within it. New elements placed in the simulation, such as additional subhaloes, cannot modify the halo potential. This could be especially problematic when considering galaxies and the adiabatic contraction that the presence of baryons is expected to produce. The second major limitation is the lack of dynamical friction that should be present in the equation of motions. Subhaloes orbiting within the expansion are missing the effect of this force that would make their orbits decay. While it is possible to add in dynamical friction analytically, this requires assuming a model of subhalo evolution to estimate the mass and size of the subhalo.

Through the application of the HEX method to a halo simulated by the *N*-body code GADGET, we have demonstrated the following:

(i) A HEX potential of a dark matter halo can approximate the halo well enough to recover the radial component of the force to within 1 per cent using only a few radial basis functions.

(ii) It is possible to integrate orbits within the expansions and reproduce overall population trends. For individual orbits, the degree of success is varied. However, it must be remembered that GADGET dynamics are not necessarily numerically perfect and therefore differences are to be expected. For orbits that are near circular and stay within the central 20 kpc of the halo, we can accurately follow their path over several dynamical time-scales.

(iii) Without dynamical friction, subhaloes follow orbits close to those of point masses. Their extended nature and tidal streams have little or no effect on their orbits. The orbits of subhaloes are not simple planar orbits but involve complicated changes in orientation and are strongly affected by encounters with the halo centre and other subhaloes.

(iv) The method can reproduce the structural evolution of individual subhaloes. To obtain similar evolution for a particular subhalo, we need to match its orbit, which requires a full potential expansion. To match the correct overall population evolution, we do not need the full expansion, but only the radial terms are required to obtain the correct radial mass distribution. Not including the angular terms greatly speeds up the force evaluation.

We have been able to introduce new objects, such as subhaloes into the HEX potential; we find an evolution consistent with that which would have taken place had the subhaloes been present in the original Aquarius simulation. The technique allows us to simulate subhaloes with much higher resolution than in the original simulation and resolve features in the tidally stripped streams in great detail.

While the HEX technique has some limitations, it offers a powerful way of improving current models of galaxy formation. The standard simple spherically symmetric profiles often used to represent the dark matter halo when modelling dynamical processes involving orbits miss important effects related to the triaxiality of haloes and the evolution of the potential. In order to build more realistic models, it is necessary, as we have shown, to use more sophisticated representations of dark matter haloes such as the ones the HEX technique offers. There is a large number of possible applications for this technique and we have briefly explored only a few of these in this paper.

REFERENCES

Abadi M. G., Navarro J. F., Fardal M., Babul A., Steinmetz M., 2010, MNRAS, 407, 435
Abramowitz M., Stegun I. A., 1964, Handbook of Mathematical Functions with Formulas, Graphs, and Mathematical Tables. Dover Press, New York
Adams F. C., Bloch A. M., 2005, ApJ, 629, 204
Allgood B., Flores R. A., Primack J. R., Kravtsov A. V., Wechsler R. H., Faltenbacher A., Bullock J. S., 2006, MNRAS, 367, 1781
Angulo R. E., Lacey C. G., Baugh C. M., Frenk C. S., 2009, MNRAS, 399, 983
Benson A. J., Lacey C. G., Frenk C. S., Baugh C. M., Cole S., 2004, MNRAS, 351, 1215
Bett P., Eke V., Frenk C. S., Jenkins A., Helly J., Navarro J., 2007, MNRAS, 376, 215
Bett P., Eke V., Frenk C. S., Jenkins A., Okamoto T., 2010, MNRAS, 404, 1137
Binney J., Tremaine S., 1987, Galactic Dynamics, 1st edn. Princeton Univ. Press, Princeton, NJ
Boylan-Kolchin M., Ma C., Quataert E., 2008, MNRAS, 383, 93
Bullock J. S., Johnston K. V., 2005, ApJ, 635, 931
Chandrasekhar S., 1943, ApJ, 97, 255
Choi J., Weinberg M. D., Katz N., 2009, MNRAS, 400, 1247
Clutton-Brock M., 1972, Ap&SS, 16, 101
Clutton-Brock M., 1973, Ap&SS, 23, 55
Debattista V. P., Moore B., Quinn T., Kazantzidis S., Maas R., Mayer L., Read J., Stadel J., 2008, ApJ, 681, 1076
Diemand J., Kuhlen M., Madau P., Zemp M., Moore B., Potter D., Stadel J., 2008, Nat, 454, 735
Frenk C. S., White S. D. M., Efstathiou G., Davis M., 1985, Nat, 317, 595
Hayashi E., Navarro J. F., Springel V., 2007, MNRAS, 377, 50
Hernquist L., 1990, ApJ, 356, 359
Hernquist L., Ostriker J. P., 1992, ApJ, 386, 375 (HO)
Kazantzidis S., Magorrian J., Moore B., 2004, ApJ, 601, 37
Law D. R., Majewski S. R., Johnston K. V., 2009, ApJ, 703, L67

Navarro J. F., Frenk C. S., White S. D. M., 1996, ApJ, 462, 563
Navarro J. F., Frenk C. S., White S. D. M., 1997, ApJ, 490, 493
Navarro J. F. et al., 2010, MNRAS, 402, 21
Ostriker J. P., Mark J., 1968, ApJ, 151, 1075
Peñarrubia J., Benson A. J., 2005, MNRAS, 364, 977
Peñarrubia J., Benson A. J., Martínez-Delgado D., Rix H. W., 2006, ApJ, 645, 240
Springel V., 2005, MNRAS, 364, 1105
Springel V. et al., 2008a, MNRAS, 391, 1685
Springel V. et al., 2008b, Nat, 456, 73
Springel V., White S. D. M., Tormen G., Kauffmann G., 2001a, MNRAS, 328, 726
Springel V., Yoshida N., White S. D. M., 2001b, Nat, 6, 79
Stadel J., Potter D., Moore B., Diemand J., Madau P., Zemp M., Kuhlen M., Quilis V., 2009, MNRAS, 398, L21
Taylor J. E., Babul A., 2001, ApJ, 559, 716
Vogelsberger M., White S. D. M., 2011, MNRAS, 413, 1419
Weinberg M. D., 1996, ApJ, 470, 715
Weinberg M. D., 1999, AJ, 117, 629
White S. D. M., Rees M. J., 1978, MNRAS, 183, 341
Zentner A. R., Bullock J. S., 2003, ApJ, 598, 49

This paper has been typeset from a T$_E$X/L^{A}T$_E$X file prepared by the author.